Journal of Electroanalytical Chemistry 765 (2016) 155–167

Contents lists available at ScienceDirect

Journal of Electroanalytical Chemistry

journal homepage: www.elsevier.com/locate/jelechem

Novel electrochemical properties of an emergent mycotoxin: sterigmatocystin

César Horacio Díaz Nieto, Adrian Marcelo Granero, María Alicia Zon *, Héctor Fernández *

Departamento de Química, Facultad de Ciencias Exactas, Físico-Químicas y Naturales, Universidad Nacional de Río Cuarto, Agencia Postal N° 3 (5800), Río Cuarto, Argentina

ARTICLE INFO

Article history:
Received 21 April 2015
Received in revised form 18 November 2015
Accepted 24 November 2015
Available online 30 November 2015

Keywords:
Mycotoxins
Sterigmatocystin
Electrochemical reduction
Cyclic and square wave voltammetries
Digital simulation

ABSTRACT

The electrochemical reduction of sterigmatocystin in acetonitrile + 0.1 M tetrabutylammonium perchlorate at glassy carbon electrodes is studied for the first time using cyclic and square wave voltammetries, and controlled-potential electrolysis. Two reduction peaks centered at −1.77 and −2.33 V vs. Ag/AgCl were found, which correspond to the formation of the radical anion and dianion, respectively. The overall electrode process was diffusion controlled. The initially formed radical anion undergoes an irreversible dimerization reaction with a rate constant of $2.06 \times 10^4\ M^{-1}\ s^{-1}$, producing a basic dimeric dianion, which is protonated by the starting molecule. An unstable dimeric reaction product was detected by UHPLC-MS/MS measurements. A value of $(3.1 \pm 0.9) \times 10^{-5}\ cm^2\ s^{-1}$ was calculated for sterigmatocystin diffusion coefficient from convoluted cyclic voltammograms. Thermodynamic and kinetics parameters were determined from digital simulation of cyclic voltammograms. Probable chemical structures for the dimer are proposed based on the results of theoretical calculations. The effect of the addition of tetrabutylammonium hydroxide, trifluoroacetic acid and water on the voltammetric signals was also investigated. The quantitative determination of sterigmatocystin was carried out by square wave voltammetry using the commercial reagent. The calibration curve was linear in the concentration range from 0.050 to 11.2 ppm, and the limits of detection and quantification were 10 and 33 ppb for signal to noise ratios of 3:1 and 10:1, respectively.

1. Introduction

Mycotoxins are toxic secondary metabolites produced by different kinds of fungi [1]. Ingestion, inhalation and/or dermal adsorption of mycotoxins can produce illness or death of animal and human being [2].

Sterigmatocystin (STEH) was first isolated in 1954 from *Aspergillus versicolor* cultures [1]. However, it has been reported that STEH can be also produced by fungal species phylogenetically and phenotypically different such as *Aschersonia*, *Aspergillus*, *Bipolaris*, *Botryotrichum*, *Chaetomium*, *Emericellai*, *Eurotium*, *Farrowia*, *Fusarium*, *Humicola*, *Moelleriella*, *Monocillium* and *Podospora* [3].

STEH is a precursor of aflatoxin B1 in the biological transformation [4]. Chemical structures of STEH and aflatoxin B1 are similar (Fig. 1). Acute toxicity, carcinogenicity and the metabolism of STEH are compared to aflatoxin B1 and other hepatotoxic mycotoxins. Thirty-three species of *Aspergillus* may produce STEH [3]. There are more species that produce STEH (55 spp) than aflatoxins (13 spp).

The International Agency for Research on Cancer (IARC) classifies STEH in the group 2B (possible human carcinogen) [5] due to its toxicological, mutagenic and carcinogenic effects in animals [6].

Although aflatoxins are considered 150–200 times more powerful than STEH, the quantities of STEH produced by some strains under optimal conditions minimize this difference [7]. Studies on STEH are mainly focused on the mechanism of toxin producing, toxin contamination and carcinogenic effects [8–10].

No country has legislation related to STEH levels permitted in food. However, some countries set STEH maximum levels allowed in some food. Thus, Czech Republic and Slovakia allow a level of 50 ppb for rice, vegetables, potatoes, flour, chicken, meat and milk, and of 20 ppb for other foods. The Department of Health of California (USA) proposes a LD_{50} of 8 μg/kg of body weight for an adult of 70 kg [11], being LD_{50} the amount of a toxic substance that kills 50% of a group of test animals [1].

Relatively high levels of STEH (in the order of ppm) were detected in housing and construction materials contaminated with *A. versicolor* [12]. The post harvest contamination of cereals with *Aspergillus* fungi involves risk to human health due to the potential production of STEH and other mycotoxins such as aflatoxin B1 and ochratoxin A [13].

STEH was found in 55 of 215 samples of different grains (barley, wheat, buckwheat, rye) in Latvia in a concentration range between 0.7 and 83 ppm [14]. There is only one report related to the presence of STEH in beer. STEH was found in 2 of 26 samples analyzed in the concentration range from 4 to 7.8 ppm [15].

A. versicolor is often present in cheese, whereas aflatoxin producing fungi as *A. flavus* and *A. parasiticus* are rarely present in this food.

* Corresponding authors.
E-mail addresses: azon@exa.unrc.edu.ar, alicia_zon@hotmail.com (M.A. Zon), hfernandez@exa.unrc.edu.ar, hfernandezster@gmail.com (H. Fernández).

http://dx.doi.org/10.1016/j.jelechem.2015.11.032
1572-6657/

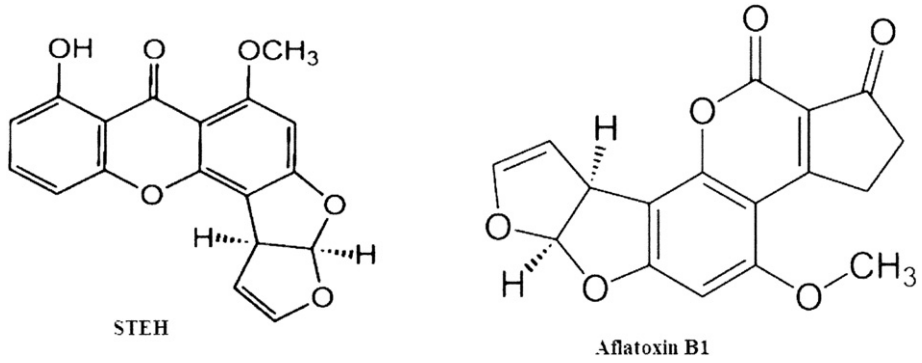

Fig. 1. Chemical structures of sterigmatocystin and aflatoxin B1.

Thus, the presence of STEH was detected in different kinds of cheese [16–19]. However, aged cheese (over six months) inhibits the production of STEH [20].

So far, the most common analytical methods used for the determination of STEH in food are: ELISA immunoassays [21–23], chromatographic methods [6] and enzyme biosensors [24,25]. However, chromatographic methods are the most widely used.

In this study, we discuss the electrochemical reduction of STEH at glassy carbon (GC) electrodes in acetonitrile (ACN) + 0.1 M tetrabutylammonium perchlorate (TBAP) using cyclic (CV) and square wave (SWV) voltammetries, and controlled potential electrolysis. We evaluated three alternative reaction mechanisms; however, one of them is the most likely based on the results of digital simulation of cyclic voltammograms and results of controlled potential electrolysis. Moreover, we also propose the most probable structures of the reaction products based on theoretical calculations. SWV was used to perform the quantitative determination of STEH using the commercial reagent.

2. Experimental

2.1. Reagents

STEH was purchased from Santa Cruz Biotechnology, USA, and used as received. ACN was Sintorgan (HPLC degree). It was first distilled over P_2O_5 (Fluka) and the distillate was dried over 3 Å molecular sieves during 48 h prior to use. TBAP (Fluka, electrochemical degree) was dried at 25 °C in a vacuum oven during 24 h and then the temperature was gradually raised to 60 °C and maintained during 24 h. Finally, it was stored in a desiccator.

Tetrabutylammonium hydroxide (TBAOH, 1.0 M in methanol) was Fluka, trifluoroacetic acid (TFA) was Sigma-Aldrich and acetone (Ac) was Sintorgan (HPLC degree). They were used as received. TBAOH solution was titrated previously to the experiments. $NaClO_4$ (Merck p.a.) was used as supporting electrolyte in controlled potential electrolysis measurements at a concentration of 0.1 M. It was first dried in a vacuum oven at room temperature and then the temperature was gradually increased to 180 °C. Then, it was stored in a desiccator.

STEH stock solutions (1.5×10^{-2} M) were prepared in ACN and kept in the refrigerator. Working solutions were prepared daily by adding aliquots of the stock solution to ACN + 0.1 M TBAP. The STEH bulk concentration (c^*_{STEH}) was varied from 3.1×10^{-8} to 5.1×10^{-3} M for voltammetric measurements. A $c^*_{STEH} = 5.6 \times 10^{-4}$ M was used for performing controlled potential electrolysis measurements. In all cases, final concentrations were calculated through UV–vis absorption measurements.

For security reasons and considering the toxicity of STEH, all solutions and experimental measurements were carried out using latex gloves and a facial mask. The residues were discarded in special bottles properly labeled. They were periodically collected by a company responsible for their final destination.

2.2. Apparatus and experimental measurements

Voltammetric and controlled potential electrolysis measurements were performed with an AutoLab PGSTAT 12 potentiostat, controlled by GPES 4.9 electrochemical software from EcoChemie, The Netherlands. In CV, the scan rate, v, was varied from 0.025 to 4 V s^{-1}. The characteristic parameters in SWV were: amplitude, ΔE_{SW} = 50 mV, staircase height, ΔE_s = 10 mV, and the frequency, f, was varied from 10 to 200 Hz.

A two-compartment Pyrex cell with a volume of 2 mL was used to perform voltammetric measurements [26]. The working electrode was a GC disk (BAS, 3 mm diameter). It was polished using 0.3 and 0.05 μm wet alumina powder (from Fischer), copiously rinsed with H_2O and sonicated in a water bath during 2 min. Finally, it was rinsed with Ac and dried under an air flow. Its electrochemical area, A, was determined through amperometric measurements [27] using a solution of 9.87×10^{-4} M $K_4[Fe(CN)_6]$ + 0.50 M KNO_3 at 25 °C. A value of 7.6×10^{-6} cm^2 s^{-1} was obtained from the literature for the $K_4[Fe(CN)_6]$ diffusion coefficient [28]. An average value of A = (0.08 ± 0.02) cm^2 was determined from four replicated measurements. The counter electrode was a large-area platinum foil (A ~ 2 cm^2). The reference electrode was Ag/AgCl (3 M NaCl). The cell for controlled potential electrolysis was one of the three-compartment types [29]. A fiberglass paper separated the working and counter electrode compartments. The working electrode was a rotating GC rod with a geometric area of 3.52 cm^2, the pseudo-reference electrode was a Ag wire and the counter electrode was a Pt foil of large area [29]. The oxygen concentration was minimized by bubbling pure argon saturated with the blank solution through the STEH solution for about 20–25 min, until the oxygen classical reduction peak at about −1.0 V disappeared [30]. Then, an argon atmosphere was kept above the solution in the cell throughout the experiment.

The positive-feedback technique was used in all experiments to compensate the solution resistance. The temperature was 25 °C.

Cyclic voltammograms were convoluted, after subtraction of background currents, by applying the method proposed by Oldham [31]. The fitting of experimental cyclic voltammograms was performed using BAS DigiSim®.

UV–vis absorption spectra were recorded using a Hewlett Packard model 8452A spectrophotometer equipped with temperature controller. Silica cells were 1 cm path length. STEH has two absorption maxima at λ = 240 nm and λ = 321 nm in ACN. In addition, an absorption peak of low absorptive appears at 280 nm. Absorption spectra recorded at different c^*_{STEH} showed that STEH satisfies to the Lambert and Beer Law. Molar extinction coefficients, ε, were ε_{240} = (3.72 ± 0.01) × 10^4 M^{-1} cm^{-1} and ε_{321} = (1.62 ± 0.01) × 10^4 M^{-1} cm^{-1}.

The UHPLC-MS/MS system consisted of an Acquity™ Ultra High Performance LC system (Waters, Milford) equipped with auto-sampler injection and pump systems (Waters, Milford). The auto-sampler vial tray was maintained at 15 °C. It was coupled to a Mass Spectrometry analyzer with a Quattro Premier™ XE Micromass MS Technologies triple

quadrupole mass spectrometer (Waters, Milford, USA). An atmospheric pressure chemical ionization (APCI) source was used for the analysis of STEH and its probable reaction product. The source was operated in a positive mode at 400 °C with N_2 as the nebulizer and the source temperature was kept at 120 °C. The corona discharge current was maintained at 2.6 μA, the extractor voltage was set at 4.0 kV and the radio frequency (RF) lens at 0.2 V. Ultrapure nitrogen was used as desolvation gas at a flow of 300 L h^{-1}. Considering that the analyses were focused on the identification of STEH and its product generated during controlled potential electrolysis, detection of both STEH and its protonated dimer molecules $[M + H]^+$ of m/z 325 and 649, respectively, was performed in the selected ion monitoring mode (SIR). The data were acquired using MassLynx Mass Spectrometry Software (Waters, Milford, USA).

The separation was performed by injecting a 10 μL sample onto an ACQUITY UPLC BEH C18 (Waters, Milford, USA) analytical column with 2.1 mm internal diameter, 50 mm length, and 1.7 μm particle size. The binary mobile phases consisted of water (A) and acetonitrile (B), both containing 0.1% (*v*/*v*) formic acid. A gradient was used at a flow rate of 0.3 mL min^{-1}. Thus, the gradient started at 60% mobile phase A with a decrease to 5% at 3 min. Initial column conditions were reached at 5.5 min, the run time was 6 min and the column was within this time reconditioned prior to the following injection. The column temperature was held at 40 °C.

Calculations to find the most probable chemical structure/s of the reaction product/s were carried out through HyperChem® software.

3. Results and discussion

Based on the molecular structure of STEH, we can predict that the mycotoxin can be electrochemically oxidized and/or reduced due to the presence of a phenolic species and a carbonyl group conjugated with two benzene rings, respectively (Fig. 1). Fig. 2 shows cyclic voltammograms recorded for the oxidation (Fig. 2a) and the reduction (Fig. 2b) of STEH. Thus, a main oxidation peak was found during the anodic potential sweep centered at about 1.6 V, and a pre-peak at about 0.9 V. The corresponding cathodic peaks were absent when the direction of the potential sweep was reversed, highlighting the presence of homogeneous chemical reaction/s coupled to the initial electron transfer reaction [27]. In addition, consecutive scans performed in the anodic potential direction showed a gradual decrease of oxidation peak currents, behavior that is expected when a phenolic species is responsible for the main oxidation peak [32], generating intermediate reaction products that polymerize and produce a gradual fouling of the electrode surface. This behavior made it difficult to study the electrochemical oxidation of STEH, at least under these experimental conditions.

On the other hand, two reduction peaks were found during the cathodic sweep, centered at −1.77 and −2.33 V, which can be associated, in principle, to the formation of the radical anion and dianion, respectively, of STEH (Fig. 2b). Consecutive scans carried out in this potential region showed a very good reproducibility, allowing performing a full study of STEH electrochemical reduction in this non-aqueous reaction medium.

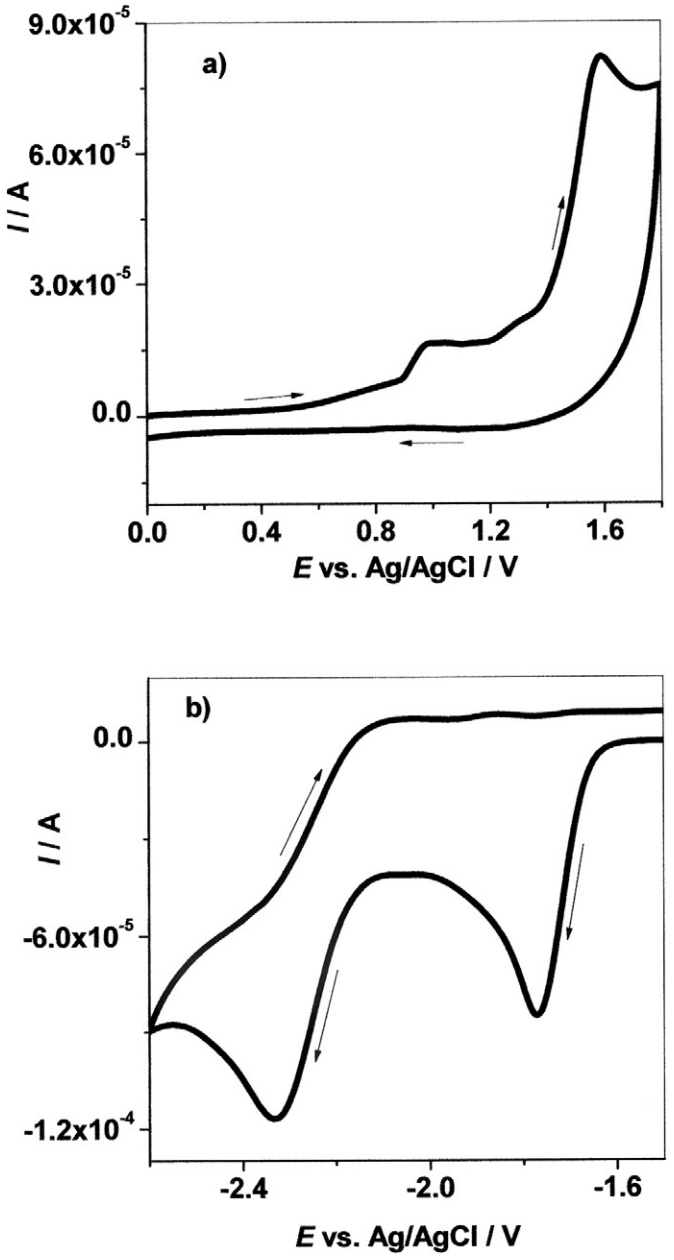

Fig. 2. a) Cyclic voltammogram recorded for STEH electrochemical oxidation in ACN + 0.1 M TBAP. $c^*_{STEH} = 1.0 \times 10^{-3}$ M, v = 0.050 V s^{-1}. b) Cyclic voltammogram recorded for STEH electrochemical reduction in the same reaction medium as a). $c^*_{STEH} = 5.1 \times 10^{-3}$ M, v = 0.100 V s^{-1}. Arrows indicate the direction of sweep potential.

3.1. Electrochemical behavior of the first STEH reduction peak

Fig. 3 shows cyclic voltammograms recorded for the first STEH electrochemical reduction peak in ACN + 0.1 M TBAP at different v, after background currents subtraction. These results show that the chemical reaction coupled to the initial electron transfer reaction has relatively slow kinetics, since the complementary anodic peak starts to define clearly at about v = 0.300 V s^{-1} when the direction of potential sweep is reversed. The relatively high stabilization of the radical anion in the time scale of voltammetric experiments could be explained by the formation of an intramolecular hydrogen bond with the –OH phenolic group present in STEH chemical structure (Fig. 1) [33]. In addition, the radical anion is also stabilized by resonance through π bonds.

Plots of cathodic peak currents, $I_{p,c,1}$, as a function of $v^{1/2}$ were linear at different STEH concentrations, with correlation coefficients (r) of 0.9984, 0.9992, 0.9992 and 0.9980 for c^*_{STEH} = 0.09, 1.2, 1.8 and 5.1×10^{-3} M, respectively. This behavior indicates that the electrode process is diffusion controlled [27].

Plots of the cathodic peak potential, $E_{p,c,1}$, as a function of log v were linear, with slopes in the range from −0.015 to −0.026 V/decade, depending on the concentration of STEH. Slopes tend to zero as the STEH concentration decreases. This behavior is predicted theoretically for E_rC_i type reactions, where $\partial E_p/\partial \log v$ varies from 0 to −0.030 V/decade with the concentration [34]. Here, E_r represents a reversible electron transfer reaction and C_i is a coupled irreversible homogeneous chemical reaction. On the other hand, a plot of $E_{p,c,1}$ vs. log c^*_{STEH} was linear, with a slope of 0.019 V/decade.

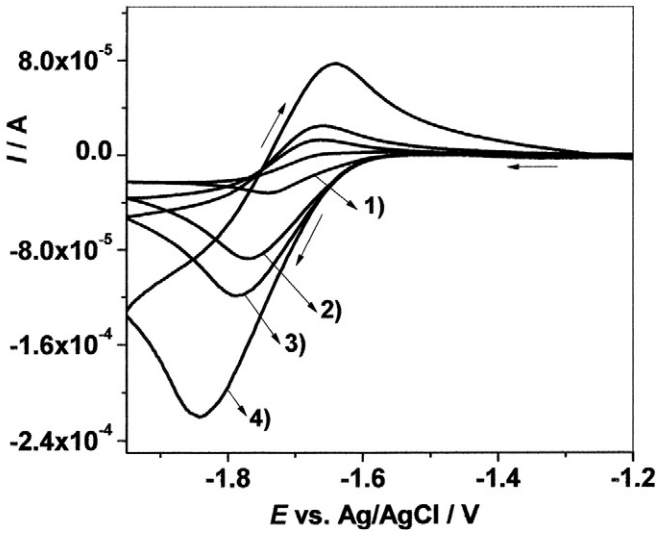

Fig. 3. Cyclic voltammograms recorded for the first STEH reduction peak in ACN + 0.1 M TBAP at different v. $c^*_{STEH} = 1.8 \times 10^{-3}$ M. v = 1) 0.050, 2) 0.500, 3) 1.0 and 4) 4.0 V s^{-1}. Arrows indicate the direction of sweep potential.

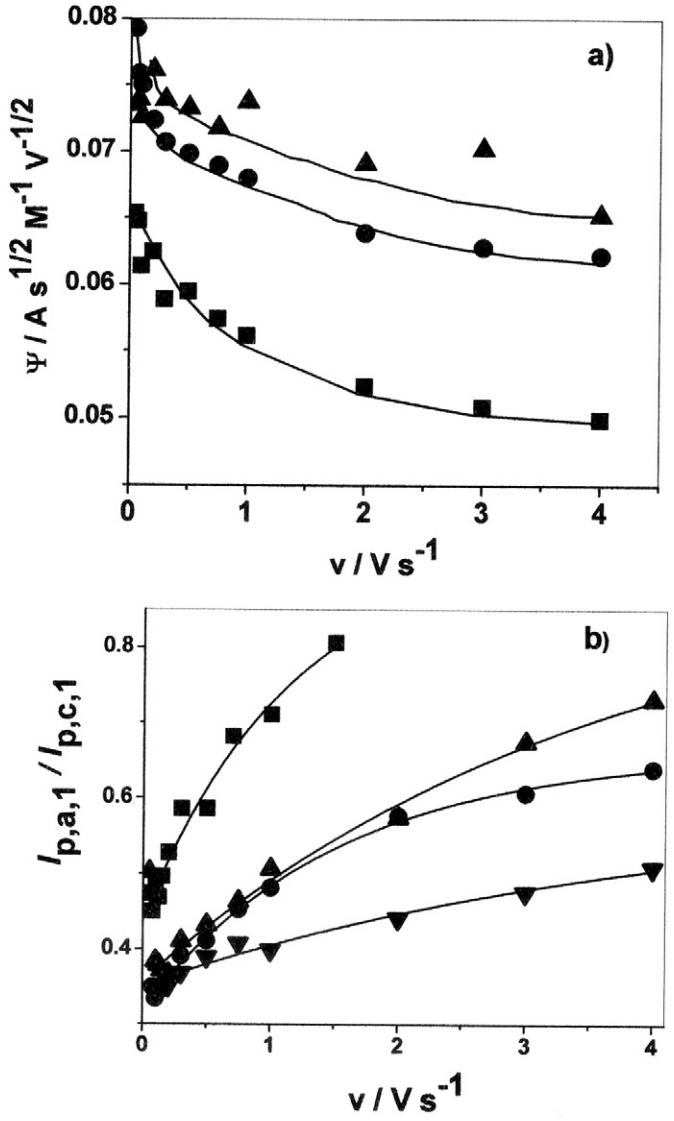

Fig. 4. a) Dependence of the current function, Ψ, with v for different STEH concentrations. c^*_{STEH} = (▲) 1.2×10^{-3}, (●) 1.8×10^{-3} and (■) 5.1×10^{-3} M. b) Dependence of $I_{p,a,1}/I_{p,c,1}$ ratio for the first reduction peak with v for different STEH concentrations. c^*_{STEH} = (■) 0.1, (▲) 1.2, (●) 1.8 and (▼) 5.1×10^{-3} M.

Fig. 4a shows plots of the current function, $\Psi = I_{p,c,1}\, v^{-1/2} c^*_{STEH}$, as a function of v for different STEH concentrations. As it can be observed, Ψ decreases as v increases, and tends to level off at v higher than 3 V s^{-1}. Ψ also reached higher values at lower c^*_{STEH} for a given scan rate. These results also suggest a mechanism of the E_rC_i type, with a second-order chemical reaction coupled to the initial electron transfer reaction [27,35,36].

A plot of the ratio between the anodic peak current ($I_{p,a,1}$) and $I_{p,c,1}$ obtained for different STEH concentrations is shown in Fig. 4b. The ratio $I_{p,a,1}/I_{p,c,1}$ is higher as the STEH concentration decreases at a given v. Moreover, this ratio tends to 1 as v is increased. This result also indicates that the kinetics of the chemical reaction coupled to the initial charge transfer reaction depends on the STEH concentration.

On the other hand, the difference between the half-peak potential and the peak potential, $E_{p,c,1} - E_{p/2,1}$, was 0.060 V in the range of scan rates from 0.025 to 1.5 V s^{-1} for low concentrations of STEH ($c^*_{STEH} < 6 \times 10^{-4}$ M). However, for STEH concentrations higher than 6×10^{-4} M, $E_{p,c,1} - E_{p/2,1}$ varied from 0.060 to 0.070 V for low scan rates, i.e., from 0.025 to 0.150 V s^{-1}. This behavior also shows that the kinetics of the homogeneous chemical reaction coupled to the initial electron transfer reaction depends on STEH concentration.

The STEH diffusion coefficient, D_{STEH}, was determined from convoluted cyclic voltammograms recorded at different v and different c^*_{STEH}. Convoluted currents did not return to zero after the cyclic scan was completed (results not shown). This behavior is expected for electrochemical systems where the product of the initial electron transfer reaction is consumed by a homogeneous chemical reaction, in principle, of the type $A + ne^- = B$, $2B \rightarrow$ products [37] (see Section 3.4), in agreement with results obtained from CV measurements [27,37]. A tentative average value for D_{STEH} was calculated considering the convolution model proposed for an EC (DIM1) reaction mechanism [37]. Thus, plots of *E* vs. log $[(I_{L,con}-I_{con})/I^{2/3}]$ obtained in the scan rate range from 0.05 to 1 V s^{-1} for different STEH concentration in the 1–5 × 10^{-3} M range were linear, where I_{con} is the convoluted current, $I_{L,con}$ is the limiting convoluted current and *I* the experimental current. The average slope was (0.116 ± 0.009) V/decade, in agreement with the one calculated through digital simulation (i.e. 0.119 V/decade, see Section 3.4.).

The slope of these plots gradually decreases for concentrations lower than about 1×10^{-3} M (i.e., 0.082 V/decade for 0.1×10^{-3} M) and tends to value close to that of a simple reversible reaction (i.e., 0.059 V/decade), showing the smallest effect of the following homogeneous chemical reaction to the electron transfer step on the overall chemical reaction. These variations are in very good agreement with results obtained by digital simulations using the most probable reaction mechanism proposed in Section 3.4.

By inserting the average slope in the expression for $I_{L,con}$ [37]:

$$I_{L,con} = n\ F\ A\ c^*_{STEH}\ D^{1/2}_{STEH} \quad (1)$$

where A is the area of the electrode and the other terms have their usual meaning, an average value of $(3.1 \pm 0.9) \times 10^{-5}$ was calculated for D_{STEH}. This value is reasonable considering the molecular weight of STEH molecule and the reaction medium [38].

3.1.1. Controlled potential electrolysis

Controlled potential electrolysis was carried out at an $E = -1.9$ V during 120 min. Cyclic voltammograms recorded during electrolysis showed several changes (Fig. 5). Therefore, a cyclic voltammogram recorded before electrolysis for the blank solution (ACN + 0.1 M $NaClO_4$) showed no peak in the potential region from 0 to −2 V (Fig. 5, line 1). STEH characteristic reduction peak was found in the presence of the mycotoxin before electrolysis, with a $E_{p,c,1} = -1.64$ V vs. Ag

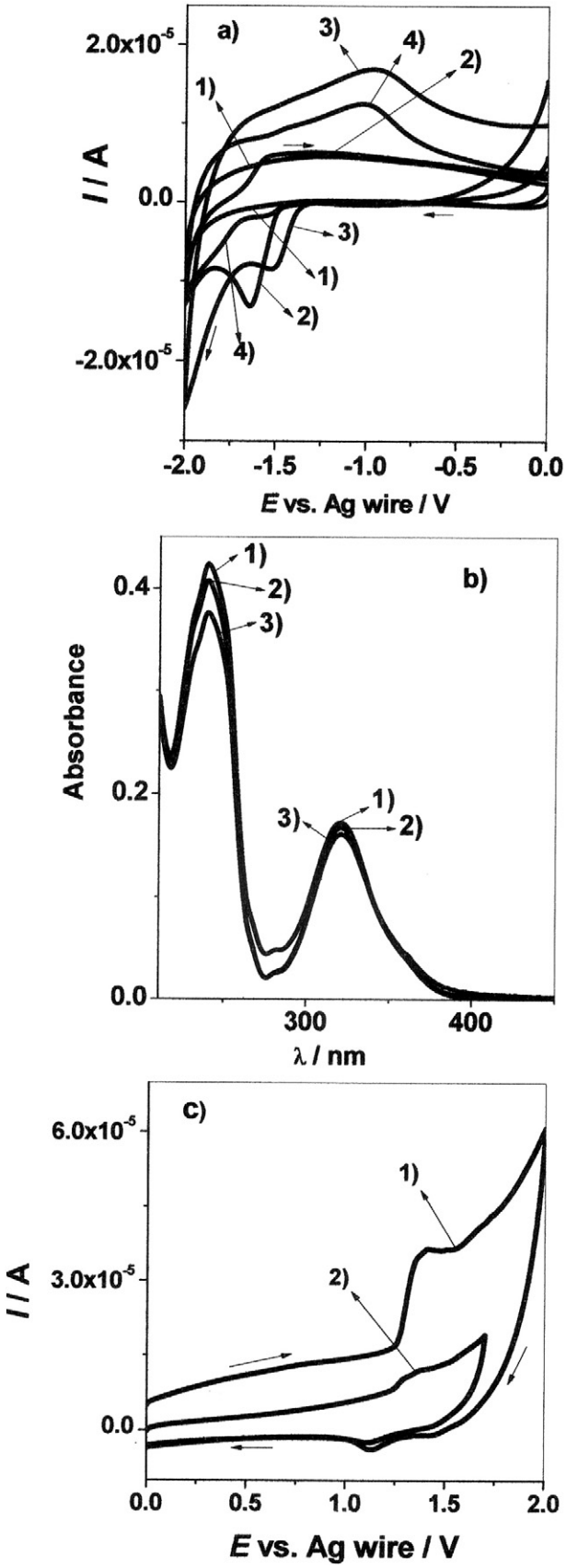

wire (Fig. 5, line 2). As electrolysis progressed, the reduction peak was shifted at less negative potentials with lower current, and an anodic peak starts to define at about −0.90 V during the reverse scan, which could be assigned to the oxidation of the homogeneous chemical reaction product/s (Fig. 5, line 3). At an electrolysis time of 120 min, the reduction peak practically disappeared and the anodic peak is well defined (Fig. 5, line 4). However, the specie responsible for this peak was unstable, as the peak current decreases and the peak disappeared in about half an hour, precluding the process of isolation and identification of the product. Based on these results, the analysis of products of controlled-potential electrolysis was performed using measures "in situ" of UHPLC-MS/MS. Therefore, Fig. 6 shows the extracted ion chromatograms (EICs) for 325 and 649 molecular masses. Before the electrolysis, at a retention time of 1.60 min, STEH was eluted (Fig. 6a). A chromatographic peak also appears at 2.13 min, which could be an impurity of STEH, which was not detected by electrochemical measurements. As expected, there was no peak corresponding to the dimer at this time.

At the end of the electrolysis, a peak appears at a molecular mass of 649 with a retention time of 4.44 min (Fig. 6b). This retention time is expected considering that the interaction forces of the dimer with the stationary and mobile chromatographic phases are larger than those of STEH. The presence of this peak confirms that the dimer proposed in the STEH electrochemical reaction mechanism described by Eqs. (15)–(18) would be one of the reduction products (see Section 3.4). However, this peak disappears in about half an hour, highlighting its instability, which is in very good agreement with the results obtained by CV measurements recorded during controlled potential electrolysis.

In addition, UV–vis spectra recorded during electrolysis showed little change in the absorption bands at λ = 240 and 321 nm, with only a slight decrease in absorbance as the electrolysis progressed (Fig. 5b). These results suggest that the chromophore group responsible for these absorption bands would be also present in the product of electrolysis. Moreover, a slight decrease in absorbance at λ = 280 nm was found. Considering that the absorption band at λ = 280 nm is a transition of n-π* type assigned to carbonyl group, the decrease in absorbance would indicate that this group is not present in the reaction product (see below).

On the other hand, cyclic voltammograms recorded after electrolysis in the potential range from 0 to 2 V showed an oxidation peak centered at 1.4 V vs. Ag/AgCl (Fig. 5c, line 1). A consecutive anodic sweep showed a marked decrease in current (Fig. 5, line 2), as expected when a phenolic species is the electroactive group [32]. From this, it is possible to infer that the product/s of controlled-potential electrolysis must have phenolic groups.

The curve *I* vs. time (t) at relatively short times (about 100 s) was used to calculate the electron number exchanged in the electrode process [39]. Thus, the following equations for the current and the charge (Q) were used:

$$I(t) = I(0)\exp(-pt) \quad (2)$$

and

$$Q(t) = Q(0)\,[1-\exp(-pt)] \quad (3)$$

Fig. 5. Controlled potential electrolysis. a) Cyclic voltammograms recorded at the blank solution (ACN + 0.1 M $NaClO_4$, line 1), and in STEH solution at different electrolysis times: 0 min (line 2), 10 min (line 3) and 120 min (line 4). b) UV–visible spectra recorded at different electrolysis times: 0 min (line 1), 10 min (line 2) and 120 min (line 3). c) Cyclic voltammograms recorded in the anodic potential region after electrolysis during the first scan (line 1), and the second scan (line 2). $c^*_{STEH} = 5.6 \times 10^{-4}$ M. v = 0.050 V s^{-1}. Arrows indicate the direction of sweep potential.

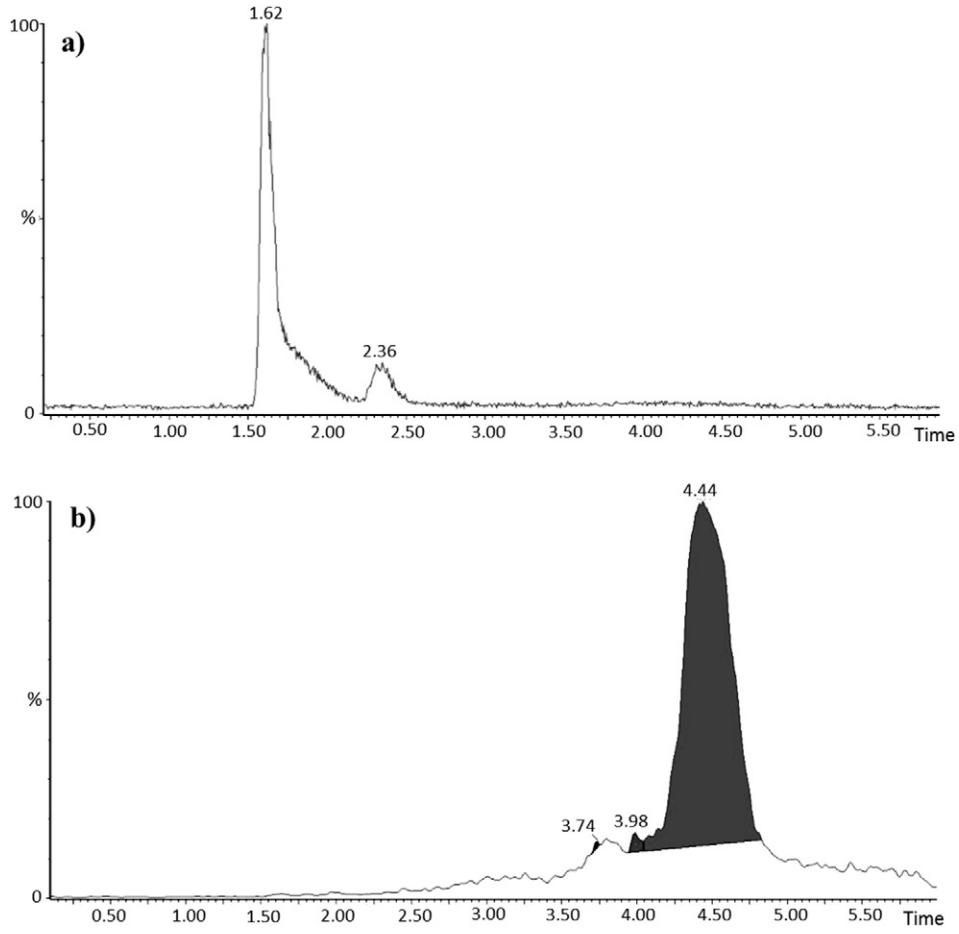

Fig. 6. Extracted ion chromatograms at (a) m/z 325 before controlled potential electrolysis and (b) at m/z 649 at the end of electrolysis.

where $I(0)$ is the current at $t = 0$, $Q(0) = nFAc^{*}_{STEH}$, and $p = m_O A/V$, being m_O the mass transfer coefficient and V the solution volume [27,39]. Q(t) can be expressed at short times as:

$$\ln Q(t) = \ln Q(0) + \ln p + \ln t \quad (4)$$

Thus, the combination of the intercept and the slope of linear plots of ln Q vs. ln t (Eq. (4)) and ln I(t) vs. t (Eq. (2)) allowed to determine n. An average value of $n = (0.5 \pm 0.1)$ was calculated from three replicated measurements.

3.2. Effect of adding TBAOH on STEH electrochemical discharge

Fig. 7a shows cyclic voltammograms recorded after the addition of different aliquots of TBAOH at the reaction medium (ACN + 0.1 M TBAP). Therefore, in the absence of the base, the two characteristic reduction peaks centered at about −1.7 and −2.3 V are clearly defined (Fig. 7a, line 1). In addition, a complementary anodic peak of the most cathodic reduction peak appears at about −2.05 V. This peak decreases as the STEH concentration increases, as it can be observed by comparison of the voltammograms of Figs. 2 and 7. As the TBAOH concentration increases, the first oxidation peak decreases and the second reduction peak shows little changes (Fig. 7a, lines 2–4). When the TBAOH concentration is about six times higher than the STEH concentration, the first reduction peak disappears and the second peak shows a slight increase in current, and a shift to slightly less negative potentials (Fig. 7a, line 5). The variation of peak currents of the first reduction peak with different base additions is shown in Fig. 7b.

Marked changes found in cyclic voltammograms by the addition of different aliquots of the base are in good agreement with changes observed in UV–vis spectra under similar experimental conditions. The addition of TBAOH, up to a concentration 2.7 times higher than the mycotoxin concentration generates the phenoxide ion, which produces large changes in absorption bands. Thus, the band at 321 nm showed a bathochromic shift to 400 nm, the band at 240 nm was slightly shifted to shorter wavelengths, and a new band appeared at 300 nm. This behavior clearly shows that an acid–base equilibrium is established in solution. The single reduction peak defined in the presence of a great excess of the base at a potential slightly less negative than the corresponding to the reduction of the anion radical (Fig. 7a, line 5) would correspond to the reduction of the phenoxide ion, the conjugate base of the substrate, which is the only species present in the reaction medium in the presence of a strong base. A similar pattern was found for the reduction of hydroxyimines, which have also phenolic species in their chemical structures [40]. Possible drawbacks due to the presence of MeOH of TBAOH solutions found in other systems [33,41] were not observed under the experimental conditions of this work for the electroreduction of STEH.

3.3. Effect of adding TFA and water on STEH electrochemical reduction

Fig. 8 shows the forward (line 1), reverse (line 2) and net (line 3) experimental currents recorded in a typical SW voltammogram for the electro-reduction of STEH in ACN + 0.1 M TBAP. These results are in good agreement with those previously described by VC. The first peak shows a clear definition of the reverse current component, even at the

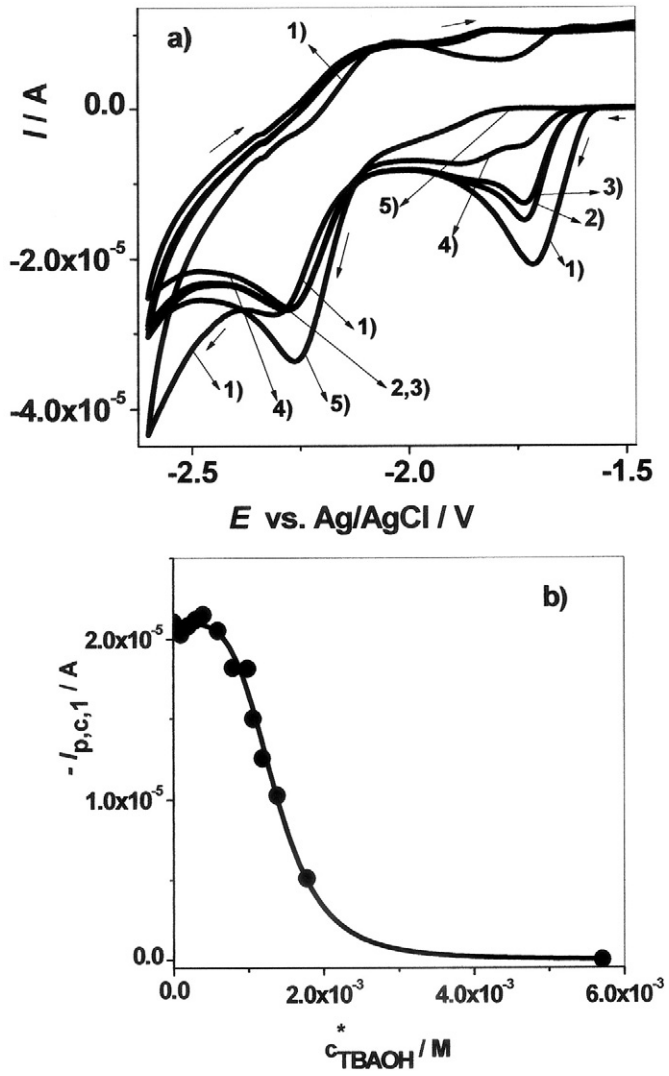

Fig. 7. a) Cyclic voltammograms recorded for STEH in the absence (line 1) and in the presence of different aliquots of TBAOH (lines 2–5). $c^*_{STEH} = 1.0 \times 10^{-3}$ M. $c^*_{TBAOH} = 1.06 \times 10^{-3}$(line 2), 1.2×10^{-3} (line 3), 1.8×10^{-3} (line 4) and 5.7×10^{-3} M (line 5). v = 0.100 V s^{-1}. Arrows indicate the direction of sweep potential. b) Dependence of $I_{p,c,1}$ with TBAOH concentration.

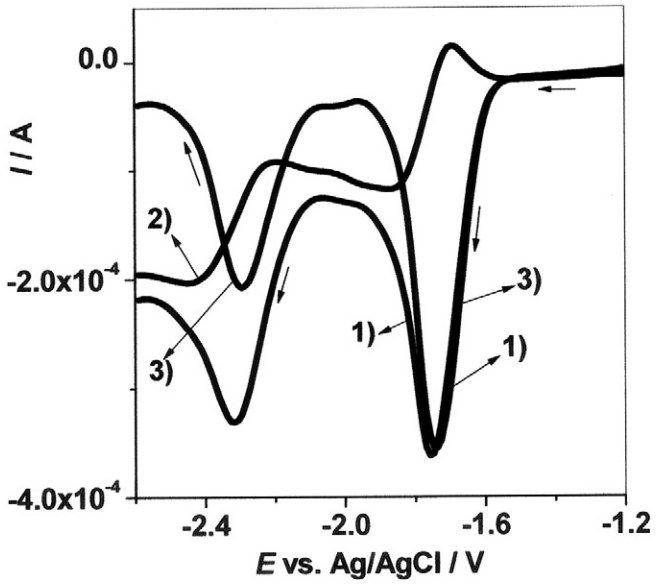

Fig. 8. Forward (line 1), reverse (line 2) and net (line 3) currents recorded for the electro-reduction of STEH in ACN + 0.1 M TBAP. $c^*_{STEH} = 5.1 \times 10^{-3}$ M. $\Delta E_{SW} = 0.050$ V, $\Delta E_s = 0.010$ V and f = 40 Hz. Arrows indicate the direction of sweep potential.

highest concentration studied and at a relatively slow scan rate, for example, v = f ΔE_s = 0.400 V s^{-1} [42]. Moreover, a small complementary anodic peak of the second reduction peak is also evident.

The net peak currents of both reduction peaks, $I_{p,n,1}$ and $I_{p,n2}$, were linear with $f^{1/2}$, with r = 0.9962 and 0.9935 for the first and the second reduction peaks, respectively, showing also a diffusion control for the electrode process [42,43].

Fig. 9 shows the net currents (I_n) recorded for the electro-reduction of STEH + 0.1 M TBAP in the absence (line 1), and in the presence (lines 2 and 3) of different aliquots of TFA. An increase in current for the first reduction peak and a slight decrease in current for the second reduction peak was found for a TFA concentration forty times lower than STEH concentration (Fig. 9, line 2). A further increase in the current of the first peak and a marked decrease in the current of the second peak was found when the concentration ratio of TFA to STEH was 0.3 (Fig. 9, line 3). TFA subsequent additions showed a new small increase in the current of the first peak and the complete disappearance of the second reduction peak (results not shown). These findings clearly indicate that the most basic electro-generated species, the dianion, is rapidly protonated in the presence of a strong acid. A similar behavior was found for the electrochemical reduction of two analogs of K-group vitamins in dimethylsulfoxide in the presence of different additions of benzoic acid [44].

When the TFA concentration was equimolar with the STEH concentration, the ratio of $I_{p,n,1}$ in the presence and in the absence of TFA was 1.9. These results indicate a change in the electrochemical reaction mechanism in the presence of a strong acid, with a consequent change in the number of electrons exchanged per mole of electrolyzed substance (see below) at potentials corresponding to the first reduction peak. It has to be indicated that the addition of TFA up to a concentration 2.7 times higher than the mycotoxin concentration produced only a slight increase in the absorbance (hyperchromic effect) mainly at λ = 240 nm.

On the other hand, we also studied the addition of water to the reaction medium, which is a weaker acid than TFA. Fig. 10a shows cyclic

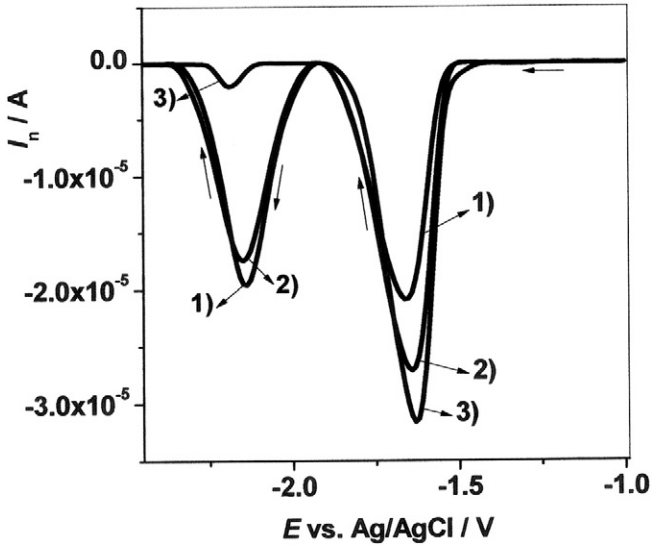

Fig. 9. Net currents recorded for STEH in ACN + 0.1 M TBAP in the absence (line 1) and in the presence of different aliquots of TFA (lines 2 and 3). $c^*_{STEH} = 1 \times 10^{-3}$ M. $c^*_{TFA} = 2.5 \times 10^{-4}$ (line 2) and 3.0×10^{-4} M (line 3). $\Delta E_{SW} = 0.050$ V, $\Delta E_s = 0.010$ V and f = 10 Hz. Arrows indicate the direction of sweep potential.

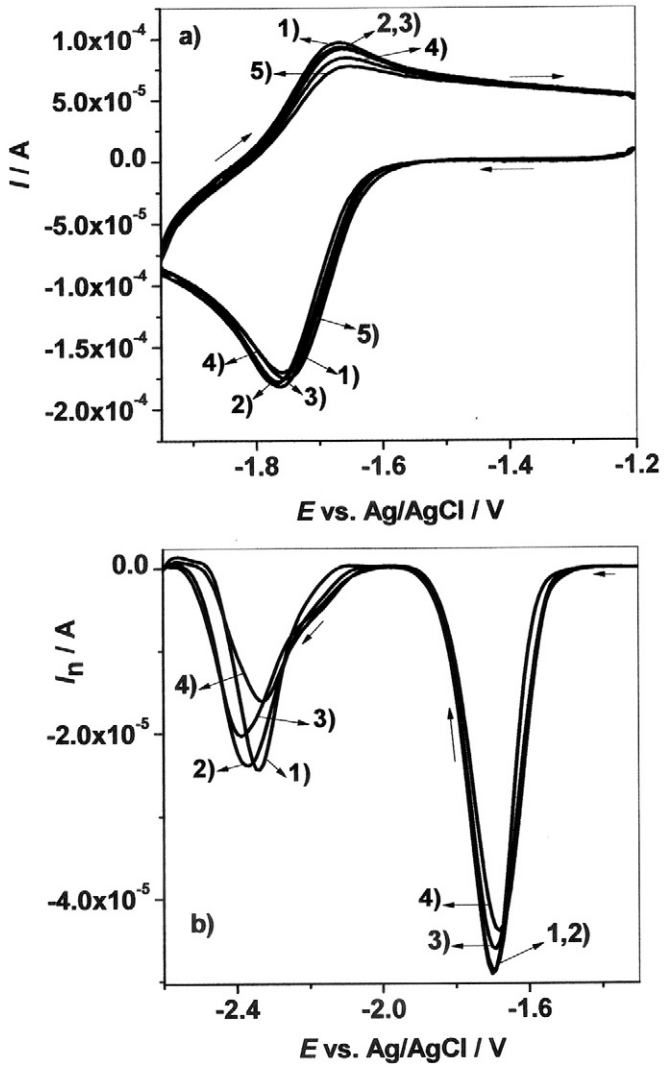

Fig. 10. a) Cyclic voltammograms of STEH in ACN + 0.1 M TBAP in the absence (line 1) and in the presence of different aliquots of water (lines 2–5). Water concentrations: 1×10^{-6} M (line 2), 5×10^{-6} M (line 3), 1.3×10^{-3} M (line 4) and 2.6×10^{-3} M (line 5). $v = 4$ V s^{-1}. b) Net square wave voltammograms of STEH in ACN + 0.1 M TBAP in the absence (line 1) and in the presence of different aliquots of water (lines 2–4). Water concentrations: 5×10^{-6} M (line 2), 1.3×10^{-3} M (line 3) and 2.6×10^{-3} M (line 4)). $c^{*}_{STEH} = 1.3 \times 10^{-3}$ M. $\Delta E_{SW} = 0.050$ V, $\Delta E_s = 0.010$ V and f = 10 Hz. Arrows indicate the direction of sweep potential.

voltammograms recorded for the first reduction peak of STEH in the absence (line 1) and in the presence of different aliquots of water (lines 2–5). No significant changes were observed in the reduction peak, even when the water concentration was twice the concentration of the mycotoxin. However, an interesting fact to mention is that the complementary anodic peak to the first reduction decreased as the water concentration increased. The role that traces of water present in organic solvents has on the electro-reduction of organic compounds has previously been discussed [45,46].

The net square wave voltammograms recorded for the two STEH reduction peaks in the absence (line 1) and after the addition of different aliquots of water (lines 2 to 4) are shown in Fig. 10b. A slight decrease in current in both reduction peaks was observed as the water concentration increased. However, the effect of water addition on STEH reduction peaks was less marked than the effect of addition of TFA, which could be explained considering the lower acidity of water compared to TFA.

3.4. Electrochemical reduction mechanism of STEH. Digital simulation

Different theoretical reaction mechanisms involving both heterogeneous (E) and homogeneous chemical (C) reactions, i.e., EC, ECE, ECEC, DIM1 (radical-radical coupling), DIM2 (substrate-radical coupling), "father–son" or self-protonation reactions, dimerization of anion radicals, etc. were used to fit experimental cyclic voltammograms [35,36,39,47–53].

It is known that when the electroactive species has an acidic proton, a probable electrochemical reduction mechanism could involve a proton transfer reaction between the initial anion radical and the starting molecule [47,48,52,53]. These reactions are called as "father–son" (starting molecule-anion radical) and give rise to a self-protonation mechanism. This electrochemical mechanism has been proved that occurs, among other compounds, during the jatropholone electrochemical reduction in N,N-dimethyl formamide + 0.1 M TBAP [53], a compound which has a phenolic –OH in its molecular structure as in the case of STEH (Fig. 1).

On the other hand, the electrochemical reduction of other organic compounds has been interpreted considering that the radical anion produced in the initial electron transfer reaction can dimerize for giving a dimer more basic than the radical anion, which can be easily protonated by the starting molecule. These reactions are called "grandparent–grandchild" because the participants are separated by one generation [49]. These reactions have been proposed for the electro-reduction of 2 fluorenecarboxaldehyde [49], some dinitro aromatic compounds [50] and two cyanopyridines [51]. Dimerization mechanisms have already been proposed for the electrochemical reduction of some xanthones [54–56]. On the other hand, the biosynthesis of dimeric xanthones has recently been described in the literature [57].

From the different theoretical reaction mechanisms used to fit experimental cyclic voltammograms, the best fits were achieved when the reaction mechanisms described by Schemes 1–3 were used as the theoretical models.

The reaction mechanisms described by Eqs. (5)–(9) (Scheme 1) and 10–14 (Scheme 2) correspond to self-protonation mechanisms. Therefore, the radical anion generated in the initial electron transfer reaction (Eq. (5) in Scheme 1, and Eq. (10) in Scheme 2) characterized by a formal potential, E^{o}_{f}, and a formal rate constant, k^{o}_{f}, is then protonated by the starting molecule (Eqs. (6) and (11) in Schemes 1 and 2, respectively, with an equilibrium constant, K_{eq}, and a homogeneous rate constant, k_f). The radical thus generated may undergo two alternative reaction pathways. It can be reduced at the electrode surface at a potential slightly lower than the own substrate (Eq. (7) in Scheme 1, characterized by $E^{o}_{f,1}$ and $k^{o}_{f,1}$) giving the corresponding anion, which is again protonated by the starting molecule to give the final product (Eq. (8), characterized by $K_{eq,1}$ and $k_{f,1}$). On the other hand, the radical generated by Eqs. (6) and (11) could react with the initial radical anion to give the

$$STEH + e^{-} \overset{E^{o}_{f},\ k^{o}_{f}}{\rightleftharpoons} STEH^{\cdot -} \quad (5)$$

$$STEH^{\cdot -} + STEH \overset{K_{eq},\ k_{f}}{\rightleftharpoons} STEH_2^{\cdot} + STE^{-} \quad (6)$$

$$STEH_2^{\cdot} + e^{-} \overset{E^{o}_{f,1},\ k^{o}_{f,1}}{\rightleftharpoons} STEH_2^{-} \quad (7)$$

$$STEH_2^{-} + STEH \overset{K_{eq,1},\ k_{f,1}}{\rightleftharpoons} STEH_3 + STE^{-} \quad (8)$$

$$3\ STEH + 2\ e^{-} \rightleftharpoons STEH_3 + 2\ STE^{-} \quad (9)$$

Scheme 1. Mechanism of self protonation.

$$2\,(STEH + e^-) \xrightleftharpoons{E_f^o,\ k_f^o} STEH^{\bullet -} \quad (10)$$

$$STEH^{\bullet -} + STEH \xrightleftharpoons{K_{eq},\ k_f} STEH_2^{\bullet} + STE^- \quad (11)$$

$$STEH^{\bullet -} + STEH_2^{\bullet} \xrightleftharpoons{K_{eq,2},\ k_{f,2}} STEH_2^- + STEH \quad (12)$$

$$STEH_2^- + STEH \xrightleftharpoons{K_{eq,1},\ k_{f,1}} STEH_3 + STE^- \quad (13)$$

$$3\,STEH + 2\,e^- \rightleftharpoons STEH_3 + 2\,STE^- \quad (14)$$

Scheme 2. Mechanism of self protonation.

anion and the parent molecule (Eq. (12), characterized by $K_{eq,2}$ and $k_{f,2}$). Finally, the anion is again protonated to give the final product (Eq. (13)). Both mechanisms described by Schemes 1 and 2 involve the exchange of 0.67 electrons per mol of electrolyzed substance.

The mechanism described by Scheme 3 corresponds to the dimerization of the radical anion. Thus, the radical anion formed in the first electron transfer reaction (Eq. (15)) dimerizes for giving a dianion dimer more basic than the anion radical (Eq. (16)), which is easily protonated by the starting molecule (Eq. (17)) giving $STEH_2$–$STEH_2$ and the conjugate base of STEH.

Based on the mechanism described by Scheme 3, the number of electrons exchanged per mole of electrolyzed substance at potentials of the first peak reduction would be 0.5, in very good agreement with the results obtained from controlled-potential electrolysis measurements (Section 3.1.1.). As previously discussed, an unstable dimeric species as the most likely STEH reduction product was found by UHPLC-MS/MS measures performed "in situ" during electrolysis (Section 3.1.1).

Fig. 11 shows experimental and fitted cyclic voltammograms for the first reduction peak at a $v = 0.100\ V\ s^{-1}$ when theoretical mechanisms used to perform the fit were those represented by Scheme 1 (Fig. 11a), Scheme 2 (Fig. 11b), and Scheme 3 (Fig. 11c). These results clearly show that the best fit was obtained when the mechanism described by Scheme 3 was chosen as the theoretical one. Based on these results, we propose as the most likely mechanism for the STEH electrochemical reduction the dimerization of the initially formed radical anion. However, besides the dimerization step, the radical anion undergoes a further competitive reduction at potentials about 0.6 V more negative than the STEH first reduction peak to give the corresponding dianion, which would be protonated by the starting molecule, residual water, and/or solvent, giving $STEH_3$. In addition, the STE^- ion (Eq. (17)) is reduced in a potential region very close to the reduction potential of the $STEH^{\bullet -}$ as it was previously described when the effect of the addition of TBAOH on voltammetric responses was analyzed (Section 3.2), indicating that the second reduction peak would have a contribution of both processes. This result agrees with the fact that a plot of the peak current ratio for both STEH reduction peaks, $I_{p,c,2}/I_{p,c,1}$ vs. v was constant (results not shown). If the second reduction peak would only correspond to the reduction of STE^- ion, the current ratio should decrease as v increases. Moreover, if only the reduction of $STEH^{\bullet -}$ contributes to the second peak, the current ratio should increase and tends to 1 as v is increased [27].

The initial electron transfer reaction (Eq. (15)) is characterized by E_f^0, k_f^o, and a cathodic transfer coefficient, α. The dimerization step (Eq. (16)) is characterized by an apparent equilibrium constant, K_{DIM}, and a homogeneous forward rate constant, $k_{f,DIM}$, and the protonation step (Eq. (17)) is characterized by an apparent equilibrium constant, $K_{eq,3}$ and a homogeneous forward rate constant, $k_{f,3}$. The dimerization step would be irreversible based on experimental results, where the anodic current of the STEH first reduction peak decreases as the scan rate decreases, in contrast to a reversible dimerization, where the anodic current increases as the scan rate decreases [51].

Fig. 12 shows experimental and fitted cyclic voltammograms for the first reduction peak at other two scan rates when the theoretical mechanism chosen to perform the fit was Scheme 3. As it can be observed, the fitting of experimental cyclic voltammograms was very good. The only parameter that was kept constant during the fitting was $\alpha = 0.5$. Other thermodynamic and kinetics parameters obtained from the best fitting were: $E_f^0 = -1.72$ V, $k_f^o = 0.044$ cm s^{-1}, $K_{DIM} = 2.08 \times 10^4\ M^{-1}$, $k_{f,DIM} = 2.06 \times 10^4\ M^{-1}\ s^{-1}$, $K_{eq} = 4.2$, and $k_f = 1.4 \times 10^5\ M^{-1}\ s^{-1}$. In addition, a value of $D_{STEH} = 1.4 \times 10^{-5}\ cm^2\ s^{-1}$ was obtained from the best fitting, which can be compared with the value determined from convoluted cyclic voltammograms (Section 3.1). The fitting of the STEH second reduction peak was more difficult to perform due to the difficulty of subtracting blank currents to very cathodic potentials.

Theoretical cyclic voltammograms based on the proposed mechanism for the STEH first reduction peak (Eqs. (15)–(18)) showed that plots of $E_{p,c,1}$ vs. log v have slopes of – (0.019 ± 0.001), – (0.021 ± 0.001), – (0.022 ± 0.001) and – (0.026 ± 0.001) for STEH concentrations of 0.1, 0.6, 1.8 and 5.1×10^{-3} M, respectively. Moreover, a plot of $E_{p,c,1}$ vs. log c^* had a slope of (0.016 ± 0.001). Slopes of E vs. log $[(I_{L,con}-I_{con})/I^{2/3}]$ plots from convoluted voltammograms obtained by simulation taking into account the mechanism represented by Eqs. (15)–(18), gave 0.119 V/decade for concentrations higher than about 1×10^{-3} M. Slopes decrease for concentrations of the electroactive substance lower than that value. For instance, a slope of 0.087 V/decade was calculated for 0.1×10^{-3} M and tends gradually to values close to that of a simple reversible reaction, i.e. 0.059 V/decade, as the concentration decreases, showing, in fact, the expected smallest effect of the following homogeneous chemical reaction to the electron transfer step on the overall chemical reaction. All these findings are in very good agreement with experimental results (see Section 3.1).

$$2\,(STEH + e^-) \xrightleftharpoons{E_f^o,\ k_f^o} STEH^{\bullet -} \quad (15)$$

$$STEH^{\bullet -} + STEH^{\bullet -} \xrightleftharpoons{K_{DIM},\ k_{f,DIM}} {}^{-}STEH\text{-}STEH^{-} \quad (16)$$

$${}^{-}STEH\text{-}STEH^{-} + 2\,STEH \xrightleftharpoons{K_{eq,3},\ k_{f,3}} STEH_2\text{-}STEH_2 + 2\,STE^- \quad (17)$$

$$4\,STEH + 2\,e^- \rightleftharpoons STEH_2\text{-}STEH_2 + 2\,STE^- \quad (18)$$

Scheme 3. Mechanism of dimerization of the radical anion.

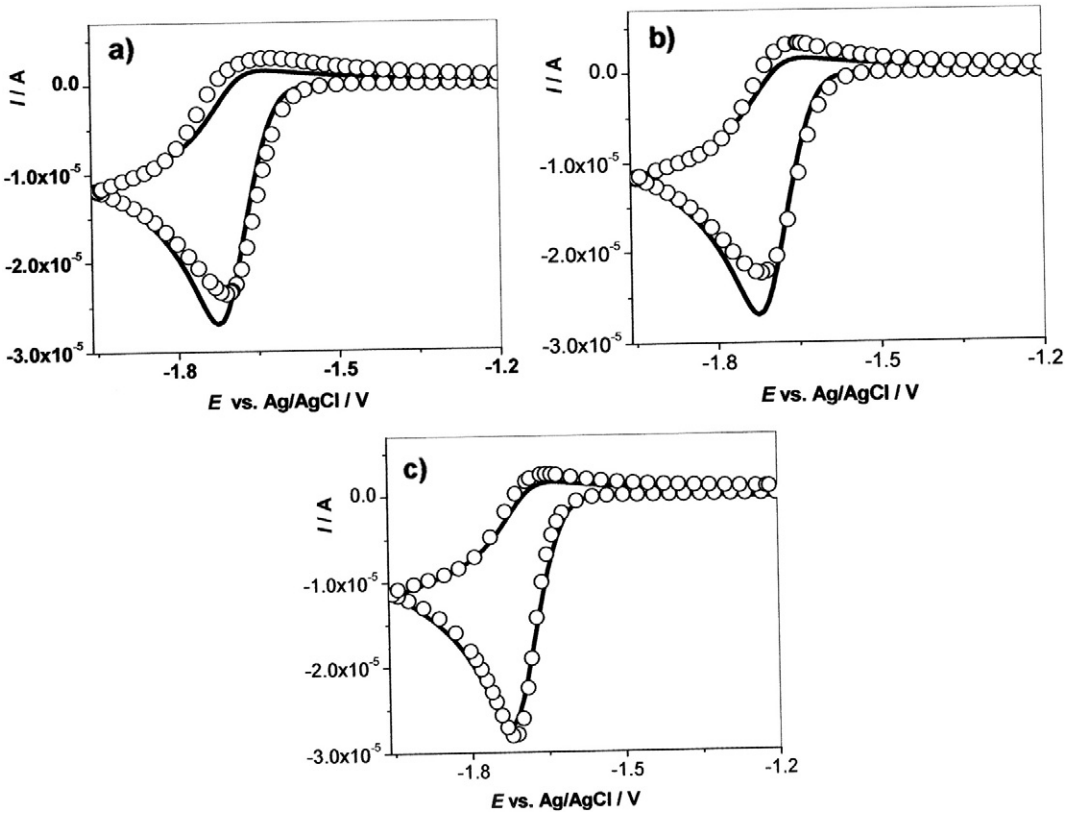

Fig. 11. Experimental (solid line) and fitted (○) cyclic voltammograms of STEH in ACN + 0.1 M TBAP using Scheme 1 (a), Scheme 2 (b), and Scheme 3 (c) as theoretical mechanisms to perform the fit. $c^{*}_{STEH} = 1.0 \times 10^{-3}$ M. v = 0.100 Vs^{-1}.

On the other hand, Eqs. (19)–(22) show the most likely STEH electro-reduction mechanism in the presence of TFA, taking into account that TFA is a stronger acid than the parent molecule.

$$2(STEH + e^{-} \rightleftarrows STEH^{\bullet -}) \tag{19}$$

$$STEH^{\bullet -} + STEH^{\bullet -} \rightleftarrows {}^{-}STEH{-}STEH^{-} \tag{20}$$

$${}^{-}STEH\text{-}STEH^{-} + 2\ TFA + 2\ e^{-} \rightleftarrows STEH_2\text{-}STEH_2 + 2\ TFA^{-} \tag{21}$$

$$\overline{2\ STEH + 2\ TFA + 2\ e^{-} \rightleftarrows STEH_2\text{-}STEH_2 + 2\ TFA^{-}} \tag{22}$$

which involve the exchanged of 1 electron per mole of electrolyzed substance at potentials corresponding at STEH first reduction peak. TFA^{-} is the conjugated base of TFA. These findings are in very good agreement with the increase of 1.9 times found in the peak current for the STEH first reduction peak in the presence of TFA and STEH equimolar concentrations (Section 3.3.).

Moreover, cyclic voltammograms recorded in the presence of different aliquots of water were also fitted using a similar mechanism as that described by Eqs. (15)–(17). The only difference was that prior to the dimerization step the following equation was included in the reaction mechanism [45]:

$$STEH^{\bullet -} + H_2O \rightleftarrows \mathrm{STEH}(H_2O)^{\bullet -} \tag{23}$$

where $\mathrm{STEH}(H_2O)^{\bullet -}$ is the radical anion complexed by a single water molecule. Under these conditions, the dimerization step occurs between an uncomplexed radical anion and a complexed radical anion. These simulations clearly put into evidence that the dimerization rate constant increases in the presence of water. These results are shown in Fig. 13, where $k_{f,DIM,W}$ and $k_{f,DIM}$ are the dimerization forward rate constants calculated in the presence and in the absence of water, respectively. These results are in very good agreement with those experimentally obtained when different water aliquots were added to the reaction medium.

Isolation and identification of protonated dimeric product from reduction of STEH was not possible because of its unstableness due to, probably, air oxidation. Thus, considering the lack of structural information we considered straightforward to perform a speculative task about the identity of the dimer.

Probable chemical structures of $STEH_2$–$STEH_2$ and $STEH_3$ are discussed below. For that, optimizing the geometry and calculations of the spin density for $STEH^{\bullet -}$ was performed using the AM1 semi-empirical method [58]. The highest spin density values are shown in Fig. 14 (sites 1 to 4). These are the most likely sites where dimerization can occur. Based on these results, we propose four probable structures for the dimer (Fig. 15). Heats of formation (ΔH_f) for probable dimers in gas phase were –259.26, −245.36, −221.10, and –238.40 kcal mol^{-1} for dimers 1, 2, 3 and 4, respectively. While values of ΔH_f would indicate higher stability of dimmers 1 and 2 in the gas phase, they can be discarded under the actual experimental conditions given the absence of an expected shift in the wave at 240 nm to shorter wavelengths, during the experiment of controlled potential electrolysis. Structures of dimers 3 and 4 explain better experimental results, particularly those of UV–vis spectroscopy obtained during the controlled potential electrolysis, since aromaticity is not lost in rings where the dimerization occurs, which indeed happens in dimers 1 and 2 (Fig. 13). Therefore, the most probable structure of the dimer would be dimer 3, considering that dimer 4 involves the formation of a peroxide bond, which, it is well known, is weak [59].

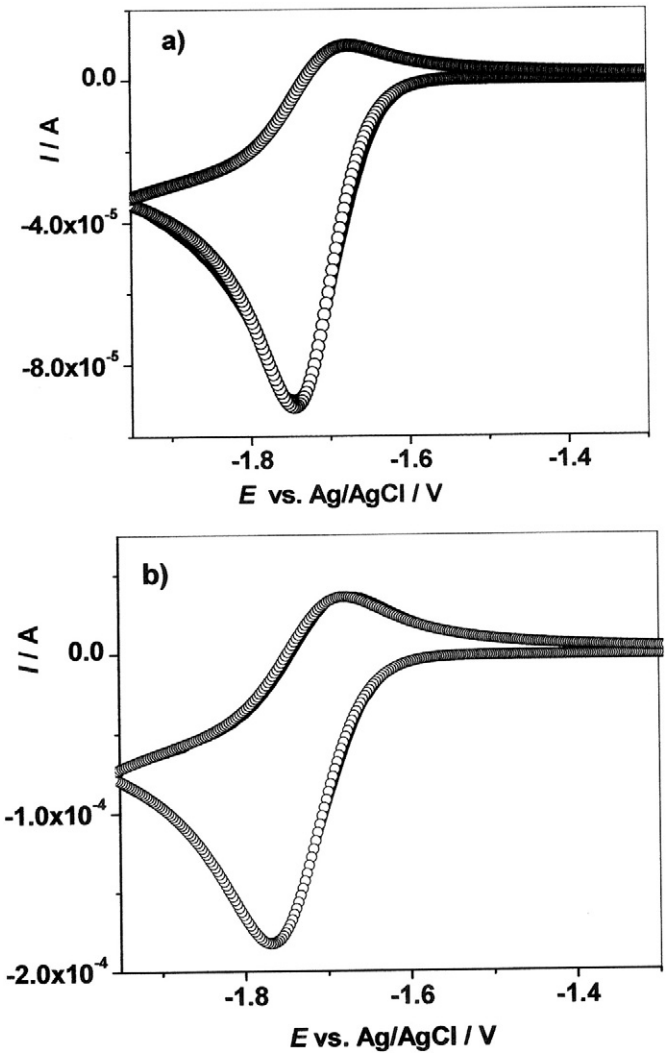

Fig. 12. Idem Fig. 10 at v: a) 1 and b) 4 Vs^{-1}. The theoretical mechanism used to perform the fitting was that indicated by Eqs. (15)–(17) (Scheme 3).

On the other hand, resonance structures of the dianion can lead to the breakage of bonds in the ring containing the carbonyl group in the STEH chemical structure (Fig. 1). Therefore, we propose the following chemical structure for $STEH_3$, which is in agreement with that proposed in the literature for the electro-reduction product of a related compound, lichexanthone in dimethylsulfoxide + 0.1 M TBAP [60].

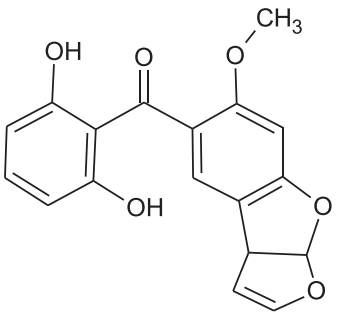

3.5. Quantitative determination of STEH

The net current — potential curve in SWV is the most useful analytical signal due to the possibility to discriminate against back-ground currents and allows obtaining low limit of detection (LOD) [42,43]. A plot of $I_{p,n,1}$ vs. c^*_{STEH} was linear in the concentration range from 0.050 to 11.2 ppm. The calibration curve can be expressed by a least-square procedure as (eleven points were taking into account, being each point the average of three replicated measurements):

$$I_{p,n,1} = (1.6 \pm 0.5) \times 10^{-7} + (6.3 \pm 0.1) \times 10^{-7} c^*_{STEH} \quad r = 0.9990 \quad (24)$$

where $I_{p,n,1}$ is expressed in amperes and c^*_{STEH} in ppm. The LOD and limit of quantification (LOQ) were 10 and 33 ppb for signal to noise ratios of 3:1 and 10:1, respectively [61].

These preliminary analytical results encourage us to study the application of pulse electrochemical methods to determine STEH in contaminated real samples in the near future as an alternative to chromatographic methods.

4. Conclusions

The electrochemical reduction of sterigmatocystin mycotoxin has been studied in acetonitrile + 0.1 M tetrabutylammonium perchlorate at glassy carbon electrodes. Results obtained by cyclic and square wave voltammetries demonstrated a complex reaction mechanism, where the radical anion formed in the initial electron transfer reaction undergoes a dimerization step to give the corresponding basic dimer dianion, which is then protonated by the parent molecule. An unstable

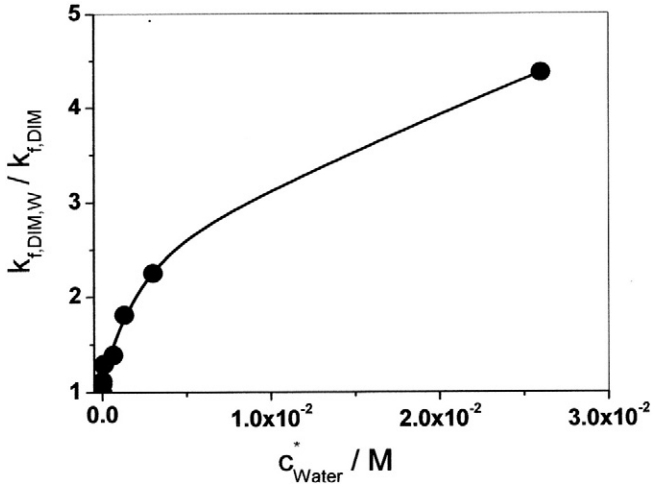

Fig. 13. Dependence of the dimerization rate constant with water concentration in the reaction medium.

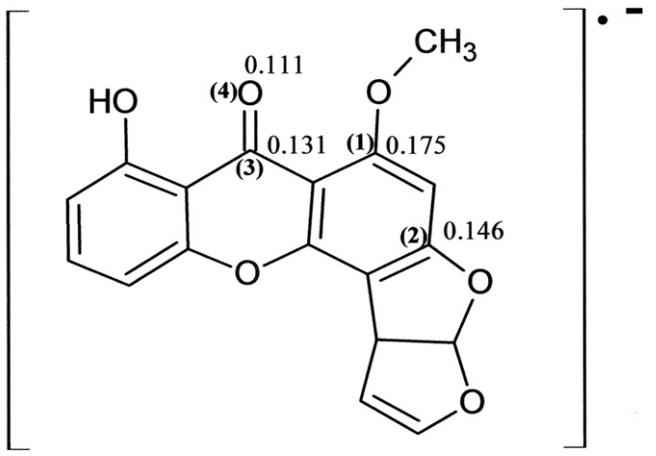

Fig. 14. Optimized geometry and calculations of the spin density for $STEH^{\bullet -}$ obtained by the semi-empirical AM1 method.

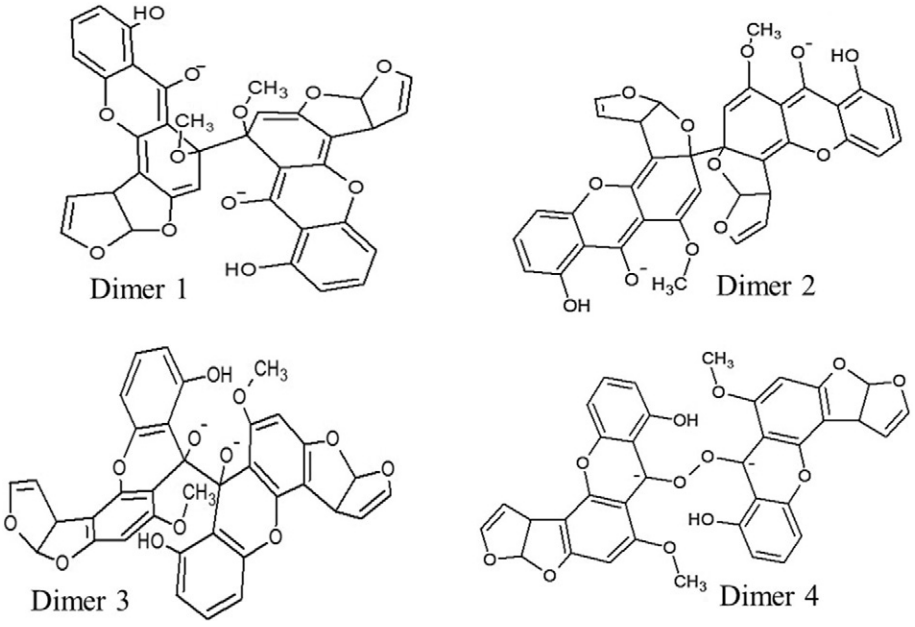

Fig. 15. Probable structures of the dimers. Dimer 1, dimer 2, dimer 3 and dimer 4 indicate that the dimer is formed by bonding of sites 1, 2, 3 and 4, respectively.

dimeric species as the most likely sterigmatocystin reduction product was found by UHPLC-MS/MS measures performed "in situ" during controlled potential electrolysis. The dianion produced in the second reduction peak is also protonated by the starting molecule. The addition of tetrabutylammonium hydroxide and trifluoroacetic acid to the reaction medium produced marked changes in voltammetric responses. Addition of water produced less pronounced changes, although increasing dimerization rate constant. Probable chemical structures of the dimer are proposed based on theoretical calculations.

Square wave voltammetry was used for quantification of the mycotoxin as a previous step for the application of this technique to determine sterigmatocystin in contaminated real samples as an alternative to chromatographic techniques in the near future.

Acknowledgments

Financial supports from Agencia Nacional de Promoción Científica y Tecnológica (FONCYT) (PICT 0916/10), Consejo Nacional de Investigaciones Científicas y Técnicas (CONICET) (PIP 112-201101-00184), Ministerio de Ciencia y Tecnología de la Provincia de Córdoba (MINCyT) (PID 050/2010), and Secretaría de Ciencia y Técnica (SECyT) from Universidad Nacional de Río Cuarto (PPI 2012-2015 Res 328/12) are gratefully acknowledged. C. H. Díaz Nieto thanks to CONICET for a doctoral fellowship. We thank the Reviewer for his/her valuable suggestions. We also thank Dra. Soledad Cerutti of the Universidad Nacional de San Luis, Argentina, who kindly helped conduct UHPLC-MS/MS experiments.

References

[1] J.M. Soriano del Castillo, Micotoxinas en Alimentos, Ediciones Díaz de Santos, España, 2007.
[2] J.I. Pitt, Australian mycotoxins newsletter, 7 (1996) 1.
[3] C. Rank, K.F. Nielsen, T.O. Larsen, J. Varga, R.A. Samson, J.C. Frisvad, Fungal Biol. 115 (2011) 406–420.
[4] V. Betina, Mycotoxins: chemical, biology and environmental aspects, vol. 9, Elsevier, Amsterdam, The Netherlands, 1989.
[5] International Agency for Research on Cancer (IARC), 2006. Available in http://www.iarc.fr
[6] A. Versilovskis, S. De Saeger, Mol. Nutr. Food Res. 54 (2010) 136–147.
[7] G.M. Shannon, O.L. Shotwell, J. Assoc. Off. Anal. Chem. 59 (1976) 963–965.
[8] E. Bloom, E. Nyman, A. Must, C. Pehrson, L. Larsson, J. Occup. Environ. Hyg. 6 (2009) 671–678.
[9] J.W. Cary, K.C. Beltz, P. Harris-Coward, M.A. Klich, Mycologia 101 (2009) 352–362.
[10] X.H. Zhan, L.Y. Xue, Carcinogenecity and biological effectiveness of sterigmatocystin, Zhonghua Bing Li Xue Za Zhi 38 (2009) 136–138.
[11] EFSA J. 11 (2013) 3254.
[12] S. Engelhart, A. Loock, D. Skularek, H. Sagunski, A. Lommel, H. Färber, M. Exner, Appl. Environ. Microbiol. 68 (2002) 3886–3890.
[13] D. Abramson, Development of mold, mycotoxins and odors in most cereals during storage, in: J. Chelkowski (Ed.), Cereal Grain: Mycotoxins, Fungi and Quality in Drying and Storage, Elsevier, Amsterdam, The Netherlands, 1991 (Ch. 6).
[14] A. Versilovslis, V. Bartkevics, V. Mikelsone, Food Chem. 109 (2008) 243–248.
[15] A. Versilovskis, S. De Saeger, V. Mikelsone, Word Mycotoxin J. 1 (2008) 161–166.
[16] M.D. Northolt, H.P. van Egmond, P.S.S. Soentoro, W.E. Deyll, J. Assoc. Off. Anal. Chem. 63 (1980) 115–119.
[17] H.P. van Egmond, Food Chem. 11 (1983) 289–307.
[18] P.M. Scott, in: H.P. van Egmond (Ed.), Mycotoxins in Dairy Products — Mycotoxigenic Fungal Contaminants of Cheese and Other Dairy Products, Elsevier Applied Science, London, 1989.
[19] F. Lund, O. Filtenborg, J.C. Frisvad, Food Microbiol. 12 (1995) 173–180.
[20] E.A.M. AbdAlla, M.M. Metwally, A.M. Mehriz, Y.H. Abu Sree, Nahrung 40 (1996) 310–313.
[21] M.R.A. Morgan, A.S. Kang, H.W.S. Chan, J. Sci. Food Agric. 37 (1986) 873–880.
[22] S. Li, P.Y. Chen, R.R. Marquart, Z. Han, J.R. Clarke, J. Agric, Food Chem. 44 (1996) 372–375.
[23] J.L. Lou, Z.Q. Guo, Z.H. Meng, Biomed. Environ. Sci. 9 (1996) 17–25.
[24] D.-S. Yao, H. Cao, S. Wen, D.-L. Liu, Y. Bai, W.-J. Zheng, Bioelectrochem. 68 (2006) 126–133.
[25] J. Chen, D. Liu, S. Li, D. Yao, Enzym. Microb. Technol. 47 (2010) 119–126.
[26] H. Fernández, M.A. Zon, J. Electroanal. Chem. 332 (1992) 237–255.
[27] A.J. Bard, L.R. Falkner, Electrochemical Methods. Fundamentals and Applications, second ed. J. Wiley & Sons, New York, USA, 2001.
[28] M.A. Zon, M.B. Moressi, L.E. Sereno, H. Fernández, Bol. Soc. Chil. Quím. 39 (1994) 139–151.
[29] A.H. Arévalo, H. Fernández, J.J. Silber, L.E. Sereno, Electrochim. Acta 35 (1990) 741–748.
[30] K. Izutsu, Electrochemistry in Nonaqueous Solutions, Wiley-VCH, New York, USA, 2002.
[31] K.B. Oldham, Anal. Chem. 58 (1986) 2296–2300.
[32] H. Lund, M.M. Baizer, Organic Chemistry: An Introduction and a Guide, Marcel Dekker, fourth ed. USA, New York, 2000.
[33] M. Gómez, F.J. González, I. González, J. Electroanal. Chem. 578 (2005) 193–202.
[34] R.S. Nicholson, I. Shain, Anal. Chem. 36 (1964) 706–723.
[35] C.P. Andrieux, L. Nadjo, J.M. Savéant, J. Electroanal. Chem. 26 (1970) 147–186.
[36] C.P. Andrieux, L. Nadjo, J.M. Savéant, J. Electroanal. Chem. 42 (1973) 223–242.
[37] J.C. Imbeaux, J.M. Savéant, J. Electroanal. Chem. 44 (1973) 169–187.
[38] D.P. Valencia, F.J. González, Electrochem. Commun. 13 (2011) 129–132.
[39] F.J. Arévalo, P.G. Molina, M.A. Zon, H. Fernández, J. Electroanal. Chem. 619-620 (2008) 46–52.
[40] A.A. Isse, A.M. Abdurahman, E. Vianello, J. Chem. Soc. Perkin Trans. 2 (1996) 597–600.
[41] J. Katsumi, T. Nakayama, Y. Esaka, B. Uno, Anal. Sci. 28 (2012) 257–265.
[42] J. Osteryoung, J.J. O'Dea, Square Wave Voltammetry, in: A.J. Bard (Ed.), Electroanalytical Chemistry, 14, Marcel Dekker, New York, USA 1987, pp. 209–308.
[43] V. Mirceski, S. Komorsky-Lovric, M. Lovric, in: F. Scholz (Ed.), Square Wave Voltammetry: Theory and Application, Springer, Leipzip, Germany, 2007.

[44] F.J. González, Electroanalysis 10 (1998) 638–641.
[45] C. Amatore, J. Pinson, J.M. Savéant, J. Electroanal. Chem. 139 (1982) 193–197.
[46] M.C. Arévalo, F. Maran, M.G. Severin, E. Vianello, J. Electroanal. Chem. 418 (1996) 47–52.
[47] C. Amatore, G. Capobianco, G. Farnia, G. Sandoná, J.-M. Savéant, M.G. Severin, E. Vianello, J. Am. Chem. Soc. 107 (1985) 1815–1824.
[48] E. Brillas, G. Farnia, M.G. Severin, E. Vianello, Electrochim. Acta 31 (1986) 759–766.
[49] N.A. Macías-Ruvalcaba, D.H. Evans, J. Electroanal. Chem. 585 (2005) 150–155.
[50] N.A. Macías-Ruvalcaba, J.P. Telo, D.H. Evans, J. Electroanal. Chem. 600 (2007) 294–302.
[51] N.A. Macías-Ruvalcaba, D.H. Evans, J. Electroanal. Chem. 660 (2011) 243–246.
[52] V.G.L. Zachetti, A.M. Granero, S.N. Robledo, M.A. Zon, C.A. DaRocha Rosa, H. Fernández, J. Braz. Chem. Soc. 23 (2012) 1131–1139.
[53] D.C. de Azevedo, J.F.C. Boodts, J.C.M. Cavalcanti, A.E.G. Santana, A.F. dos Santos, E.S. Bento, J. Tonholo, M.O.F. Goulart, J. Electroanal. Chem. 466 (1999) 99–106.
[54] W.E. Whitman, L.A. Wiles, J. Chem. Soc. (1956) 3016–3019.
[55] M.K. Kalinowski, Z.R. Grabowski, B. Pakula, Trans. Faraday Soc. 62 (1966) 918–925.
[56] M.K. Kalinowski, Z.R. Grabowski, Trans. Faraday Soc. 62 (1966) 926–934.
[57] T. Wezeman, S. Bräse, K.-S. Masters, Nat. Prod. Rep. 32 (2015) 6–28.
[58] M.J.S. Dewar, E.G. Zoebisch, E.F. Healy, J.J.P. Stewart, J. Am. Chem. Soc. 107 (1985) 3902–3909.
[59] T.W.G. Solomons, Fundamental of Organic Chemistry, J. Wiley & Sons, USA, 1982 306.
[60] A.E. Carvalho, G.B. Alcantara, S.M. Oliveira, A.C. Micheletti, N.K. Honda, G. Maia, Electrochim. Acta 54 (2009) 2290–2297.
[61] D.A. Skoog, F.J. Holler, T.A. Nieman, Principios de Análisis Instrumental, fifth ed. Mc Graw Hill, Madrid, España, 2001.